Monthly Notices of the ROYAL ASTRONOMICAL SOCIETY

MNRAS **508,** 1756–1767 (2021) https://doi.org/10.1093/mnras/stab2708
Advance Access publication 2021 September 21

# Radiation hydrodynamical simulations of the birth of intermediate-mass black holes in the first galaxies

Muhammad A. Latif [1]★ Sadegh Khochfar,[2] Dominik Schleicher[3] and Daniel J. Whalen[4,5]

[1]*Physics Department, College of Science, United Arab Emirates University, Al-Ain 15551, UAE*
[2]*Institute for Astronomy, University of Edinburgh, Royal Observatory, Blackford Hill, Edinburgh EH9 3HJ, UK*
[3]*Astronomy Department, Universidad de Concepción, Barrio Universitario, Concepción Casilla 160-C, Chile*
[4]*Institute of Cosmology and Gravitation, University of Portsmouth, Portsmouth PO1 3FX, UK*
[5]*Ida Pfeiffer Professor, University of Vienna, Department of Astrophysics, Tuerkenschanzstrasse 17, Vienna A-1180, Austria*

Accepted 2021 September 16. Received 2021 September 10; in original form 2020 December 16

## ABSTRACT

The leading contenders for the seeds of $z > 6$ quasars are direct-collapse black holes (DCBHs) forming in atomically cooled haloes at $z \sim 20$. However, the Lyman–Werner (LW) UV background required to form DCBHs of $10^5$ $M_\odot$ are extreme, about $10^4$ $J_{21}$, and may have been rare in the early universe. Here we investigate the formation of intermediate-mass black holes (IMBHs) under moderate LW backgrounds of 100 and 500 $J_{21}$, which were much more common at early times. These backgrounds allow haloes to grow to a few $10^6$–$10^7$ $M_\odot$ and virial temperatures of nearly $10^4$ K before collapsing, but do not completely sterilize them of $H_2$. Gas collapse then proceeds via Ly$\alpha$ and rapid $H_2$ cooling at rates that are 10–50 times those in normal Pop III star-forming haloes, but less than those in purely atomically cooled haloes. Pop III stars accreting at such rates become blue and hot, and we find that their ionizing UV radiation limits their final masses to 1800–2800 $M_\odot$ at which they later collapse to IMBHs. Moderate LW backgrounds thus produced IMBHs in far greater numbers than DCBHs in the early universe.

**Key words:** black hole physics – galaxies: high-redshift – dark ages, reionization, first stars – early universe – cosmology: theory.

## 1 INTRODUCTION

The discovery of quasars at $z > 7$ (Mortlock et al. 2011; Wu et al. 2015; Bañados et al. 2018; Yang et al. 2020) poses significant challenges to current paradigms of structure formation, because it is not fully understood how supermassive black holes (SMBHs) formed less than a Gyr after the big bang (Volonteri 2010; Haiman 2013; Latif & Ferrara 2016; Inayoshi, Visbal & Haiman 2019; Woods et al. 2019). A number of origins have been proposed for high-$z$ quasars such as the BHs of Pop III stars at $z \sim 25$ (10–500 $M_\odot$; Madau, Haardt & Dotti 2014; Volonteri, Silk & Dubus 2015), runaway stellar collisions in marginally enriched haloes at $z \sim 15$–$20$ (1000–4000 $M_\odot$; Devecchi & Volonteri 2009; Sakurai et al. 2017; Boekholt et al. 2018; Reinoso et al. 2018), and direct-collapse black holes (DCBHs) in atomically cooled haloes at $z \sim 15$–$20$ ($\sim 10^5$ $M_\odot$; Latif et al. 2013b; Schleicher et al. 2013; Regan, Johansson & Wise 2014; Chon, Hosokawa & Yoshida 2018; Smidt et al. 2018; Maio et al. 2019).

DCBHs form when primordial haloes grow to masses $\gtrsim 10^7$ $M_\odot$ and virial temperatures of $\sim 10^4$ K without having previously formed a star, because they are immersed in strong Lyman–Werner (LW) UV backgrounds that destroy their $H_2$ (e.g. Latif et al. 2014b; Agarwal & Khochfar 2015; Agarwal et al. 2019) or in supersonic baryon streaming flows that prevent star formation (SF) even if $H_2$ is present (Tseliakhovich & Hirata 2010; Greif et al. 2011; Stacy, Bromm & Loeb 2011; Schauer et al. 2017). Temperatures of $10^4$ K activate Ly$\alpha$ cooling that triggers rapid baryon collapse at up to 1 $M_\odot$ yr$^{-1}$ (Wise, Turk & Abel 2008; Regan & Haehnelt 2009). Stellar evolution calculations have shown that such flows can create stars with masses $\gtrsim 10^5$ $M_\odot$ that collapse to DCBHs via the general relativistic instability (Hosokawa et al. 2013; Umeda et al. 2016; Woods et al. 2017; Haemmerlé et al. 2018a,b). DCBHs are the leading candidates for the seeds of the first quasars, because they form in dense environments in haloes that can retain their fuel supply even when it is heated by the BH (Whalen, Abel & Norman 2004; Alvarez, Wise & Abel 2009; Whalen & Fryer 2012; Johnson et al. 2013; Smith et al. 2018; Zhu et al. 2020).

The accretion rates of 0.1–1 $M_\odot$ yr$^{-1}$ required to build up $10^5$ $M_\odot$ stars can only be sustained by atomic cooling, not $H_2$, and the LW backgrounds required for the complete extinction of $H_2$ in haloes are extreme, as much as a few $10^4$ $J_{21}$, where $J_{21} = 10^{-21}$ erg s$^{-1}$ cm$^{-2}$ Hz$^{-1}$ sr$^{-1}$ (Sugimura, Omukai & Inoue 2014; Latif et al. 2015). But there is a growing body of work that suggests that massive stars can form even in the presence of minute amounts of $H_2$ shielded deep in the cores of haloes exposed to more modest LW fluxes. Safranek-Shrader et al. (2012) examined the collapse of a $3 \times 10^7$ $M_\odot$ halo in a LW background of 100 $J_{21}$ and found that cooling at its center was still governed by $H_2$ and produced a sink particle with a mass of $\sim$1100 $M_\odot$. Latif et al. (2014c) also found that 100–10 000 $M_\odot$ primordial stars could form in haloes immersed in moderate LW fluxes (see also Latif & Volonteri 2015).

Until recently, simulations of baryon collapse in atomically cooled haloes ignored radiative feedback from stars at their centers, because stellar evolution models predicted that they were likely cool and red, and therefore not strong sources of ionizing UV flux capable of

★ E-mail: latifne@gmail.com

halting accretion on to the star (although pressure due to outflowing Ly$\alpha$ cooling radiation may could affect flows deep in the core of the halo; Smith et al. 2017). The first models to incorporate stellar feedback found it had little effect on the growth of the star on au scales over times of a few years (Ardaneh et al. 2018; Luo et al. 2018). Chon et al. (2018) and Regan & Downes (2018b) followed the collapse of haloes in LW backgrounds of 100 and 1000 $J_{21}$ for a few hundred kyr and also found that radiation from stars did not suppress accretion. However, the presence of even small mass fractions of $H_2$ in haloes in LW backgrounds of these magnitudes can reduce infall rates by 1–2 orders of magnitude, down to 0.005–0.03 $M_\odot$ $yr^{-1}$. Stars growing at the low end of this range have been found to become blue and hot in stellar evolution models, with ionizing UV fluxes that could at least partially quench accretion (Haemmerlé et al. 2018a). How such feedback governs the final masses of stars in these backgrounds is not yet known.

The original simulations of atomically cooled haloes that proceeded from cosmological initial conditions did not exhibit fragmentation or the formation of dense clumps that could later become multiple massive stars (although see Bromm & Loeb 2003). Later studies at higher resolution revealed that atomically cooled gas fragmented on au scales, but could only follow the evolution of the clumps for a few tens of years, and could not determine if they later became stars or were subsumed by the disc at later times (Becerra et al. 2015, 2018). Regan & Downes (2018a,b) and Chon et al. (2018) studied fragmentation at somewhat lower resolutions out to a few hundred kyr and found that some clumps persisted for long times, but could not determine their final fates. Also Regan & Downes (2018a) simulated a single rare halo of $\sim 10^7$ $M_\odot$ at z = 24.7, while we here explore typical haloes forming in high-z universe. Suazo et al. (2019) followed the collapse of atomically cooled haloes at intermediate resolutions in moderate LW backgrounds for ∼600 kyr, longer than previous studies but still well short of the collapse of the stars. Inflow rates lasting for the times required to actually form DCBHs have only recently been confirmed to occur in numerical simulations (Latif, Khochfar & Whalen 2020; Patrick et al. 2020; Regan et al. 2020). Although binary and multiple DCBH systems formed in all three studies, which holds important implications for the detection of DCBH mergers by the Laser Interferometer Space Antenna (LISA) in coming decades, they did not include radiation from the stars and may not ultimately be self-consistent.

Here, we investigate the prospect of massive BH seeds formation in typical primordial haloes ranging in mass from $1.5 \times 10^6$ $M_\odot$ to $2.3 \times 10^7$ $M_\odot$ in LW backgrounds of 100 $J_{21}$ and 500 $J_{21}$, which were much more common in the primordial universe than those required for complete photodissociation of $H_2$. Our simulations are evolved for up to ∼900 kyr, approximately three times longer than in comparable studies, and include radiative feedback from the stars coupled to hydrodynamics and primordial gas chemistry. We describe our simulations in Section 2, present our results in Section 3, and conclude in Section 4.

## 2 NUMERICAL METHOD

Our simulations were performed with the Enzo adaptive mesh refinement (AMR) cosmology code (Bryan et al. 2014). We initialize our runs with cosmological initial conditions generated by MUSIC (Hahn & Abel 2011) at $z = 150$ with cosmological parameters taken from Planck 2016 data: $\Omega_M = 0.308$, $\Omega_\Lambda = 0.691$, $\Omega_b = 0.0223$, and $h = 0.677$ (Planck Collaboration XIII 2016). Our simulation volume is 1 cMpc $h^{-1}$ on a side with a top grid resolution of $256^3$ and two additional nested grids each with a resolution of $256^3$ that span 20 per cent of the top grid. We place the halo of interest at the center of the box and allow up to 16 additional levels of refinement during the runs to achieve resolutions of up to ∼300 au. We split dark matter (DM) particles in this region into 13 child particles, which produces an effective DM resolution of 5 $M_\odot$ $h^{-1}$. Beginning at $z = 150$, we refine on Jeans length, baryonic overdensity, and particle mass resolution, as in Latif & Khochfar (2020) and Latif et al. (2020). The Jeans length is resolved by at least 32 cells in our models.

We introduce sink particles that represent Pop III stars in cells where the maximum refinement level is reached, typically at densities of $\geq 10^{-16}$ g $cm^-3$. Our criterion for sink particle formation is based on SmartStars (Regan & Downes 2018b). A sink particle is allowed to form in a grid cell when meeting the following criteria: (I) the grid cell is at the maximum refinement level; (II) the cell density is higher than the Jeans density; (III) the flow is convergent; (IV) the cooling time is shorter than the free-fall time; (V) the cell is at a local minimum of the gravitational potential. It can accrete gas from a radius of 4 cells and merges with the most massive particle within the accretion radius. Our recipe for accretion is based on the mass influx at the accretion sphere and we use the averaged accretion rate over 1 kyr as the actual accretion rate.

Stars are treated as red and cool if their accretion rates exceed 0.04 $M_\odot$ $yr^{-1}$ and blue and hot if they accrete below this rate. We assign a $10^5$ K blackbody spectrum to blue stars $M_\odot$ (Schaerer 2002) and a 5500 K blackbody spectrum to red stars (Hosokawa et al. 2013), assuming in both cases that their luminosities scale with their masses. Consequently, as stars grow in mass they become more luminous and produce strong feedback. Photons from stars are propagated throughout the simulation volume with the MORAY raytracing radiation transport package, which is self-consistently coupled to hydrodynamics and non-equilibrium primordial gas chemistry in Enzo (Wise & Abel 2011). Each star is a point source of both ionizing and dissociating radiation whose spectrum is partitioned into five energy bins: 2.0 eV and 12.8 eV, which can destroy $H^-$, $H_2$, and $H_2^+$, and three ionizing energies, 14.0 eV, 25.0 eV, and 200.0 eV. We use SEDOP to populate the last three bins which allows us to compute the optimum number of energy bins required to model radiation above the hydrogen ionization limit (Mirocha et al. 2012). The energy fractions of 0.3261, 0.1073, 0.3686, 0.1965, and 0.0 are used in bins 1–5, respectively, which are determined from table 4 of Schaerer (2002).

We employ a non-equilibrium primordial chemistry solver (Abel et al. 1997) to evolve the nine primordial species in our runs: H, $H^+$, $H^-$, He, $He^+$, $He^{++}$, $H_2$, $H_2^+$, $e^-$. Our simulations include $H_2$ cooling, collisional excitation, and ionization cooling by H and He, bremsstrahlung cooling, and recombinational cooling. Uniform LW backgrounds of 100 or 500 $J_{21}$ are turned on at $z = 30$ to suppress SF in minihaloes and self-shielding of $H_2$ is approximated by fits from Wolcott-Green, Haiman & Bryan (2011). Such flux is higher than the expected background at this redshift but could be provided by star-forming galaxies in the vicinity of the halo. In such scenarios the LW flux becomes almost uniform in the target halo (also see Agarwal et al. 2017). We ignore radiation pressure due to photoionizations, which could facilitate H II region breakout by imparting momentum to the surrounding gas. Whalen & Norman (2008) examined the impact of radiation pressure at lower densities and found that they amount to at most 20 per cent of the ionized gas pressure. In fact, we performed a test simulation by including radiation pressure and found the stellar masses to be similar to the case without radiation pressure. We therefore conclude that radiation pressure will not strongly affect our results.

**Table 1.** Virial masses, collapse redshifts, and LW backgrounds for the six haloes in our study. The final masses of the stars in each halo are listed in column 5.

| Halo | $z$ | Mass ($M_\odot$) | $J_{21}$ | Stars ($M_\odot$) |
|---|---|---|---|---|
| H1 | 16.5 | $7.5 \times 10^6$ | 100 | 196, 97, 27, 2775 |
| H2 | 14.5 | $1.7 \times 10^7$ | 500 | 1668,10, 8683 |
| H3 | 22.8 | $1.5 \times 10^6$ | 100 | 2743 |
| H4 | 18.5 | $5.4 \times 10^6$ | 500 | 60, 94,25, 2638 |
| H5 | 13.3 | $1.3 \times 10^7$ | 100 | 346, 520, 1161, 2079 |
| H6 | 13.31 | $1.7 \times 10^7$ | 500 | 546,1955 |

## 3 RESULTS

### 3.1 Halo properties

We have simulated six haloes, labelled H1, H2, H3, H4, H5, and H6, whose masses and collapse redshifts are listed in Table 1. Our haloes form in different environments with DM overdensities of 10–100 times the cosmic mean and also have a variety of merger histories. We compute the DM overdensity by calculating the mean DM density in a radius that is 10 times the virial radius of the halo and compare it to the cosmic mean in a volume of 1 $(\mathrm{Mpc\,h^{-1}})^3$. This allows us to estimate the environment of the halo. H1–H6 have DM overdensities of 10, 50, 90, 70, 100, and 65, respectively. Haloes H2, H4, and H5 have undergone a major merger, while the others have grown mainly through accretion from the cosmic web and minor mergers. The merger ratios are for H2, H4, and H5 are 1:3, 1:5, and 1:2, respectively. The halo spins for H1–H6 are 0.02, 0.016, 0.029, 0.012, 0.038, and 0.032, respectively. Their spin parameters vary from 0.015 to 0.04, which is close to the mean value of 0.02 expected for the halo spin distribution at $z \sim 15$ (Davis & Natarajan 2009).

### 3.2 Initial collapse

Baryon collapse is suppressed by LW radiation in all six haloes until they reach masses of at least $10^6$ $M_\odot$, and in most cases $10^7$ $M_\odot$ (Latif & Khochfar 2019). However, as shown in the temperature profiles in Fig. 1, once collapse begins it is mediated by both Ly$\alpha$ and $H_2$ cooling. At the onset of SF, atomic cooling dominates down to radii of a few pc, where the gas is at temperatures of ∼8000 K due to the dissociation by external UV radiation , but $H_2$ cooling, which produces temperatures of 300–1000 K, dominates at radii less than 1 pc. This can also be seen in the $H_2$ mass fractions, which can exceed $10^{-3}$ below 1 pc, because they are self-shielded from the external background. The $H_2$-cooled core of the halo is at higher temperatures than those in normal Pop III star-forming haloes, which are typically 200–300 K, because they are subject to higher mass loading from atomic cooling in the surrounding gas. Overall, H5 has the higher $H_2$ mass fraction and lower temperature than all haloes because of the larger cooling rate. In comparison with H5, H6 has a lower $H_2$ fraction and higher temperature.

The two-phase temperature structure in our haloes is due to the LW background, which allows them to grow to larger masses and higher virial temperatures before collapsing, but does not completely sterilize them of $H_2$. Because their cores are at higher temperatures than those of normal Pop III star-forming haloes, $H_2$ cooling and formation rates, which peak at 1000–2000 K, are much higher there (O'Shea & Norman 2007). This leads to central accretion rates that are much higher than those in normal minihaloes but less than

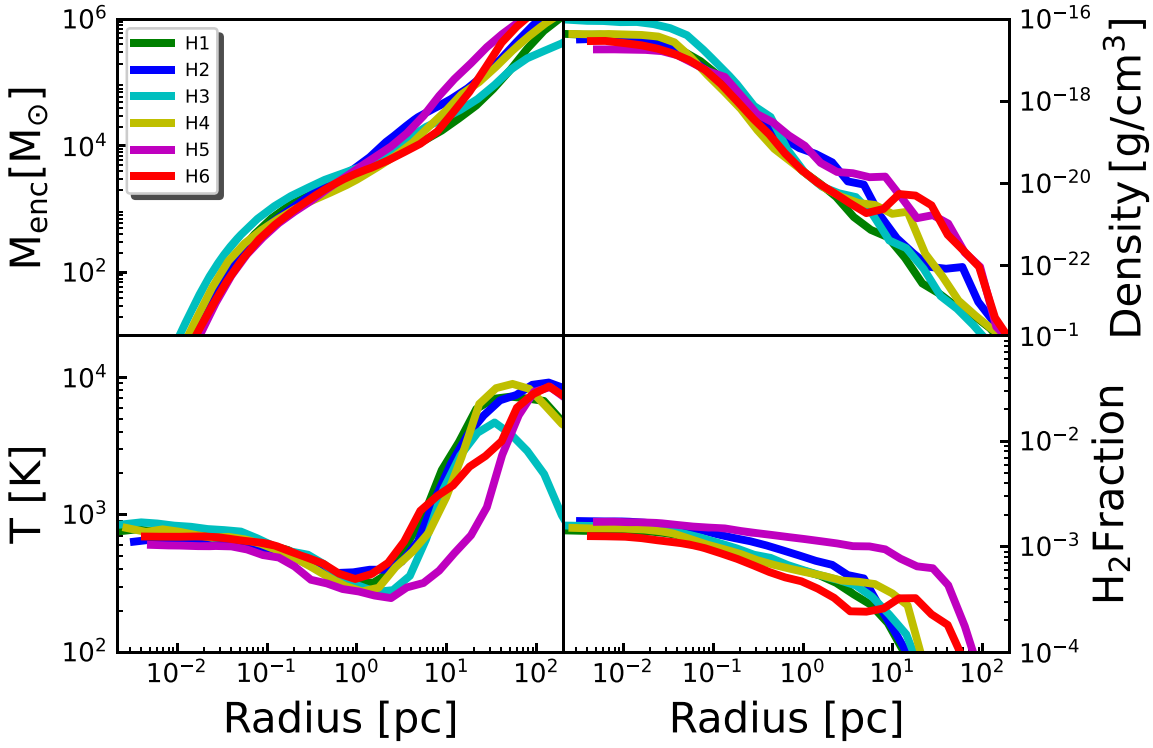


**Figure 1.** Spherically averaged radial profiles of density, temperature, enclosed mass, and $H_2$ mass fraction at the onset of SF. Green, blue, cyan, yellow, magenta, and red colours are haloes H1, H2, H3, H4, H5, and H6, respectively.

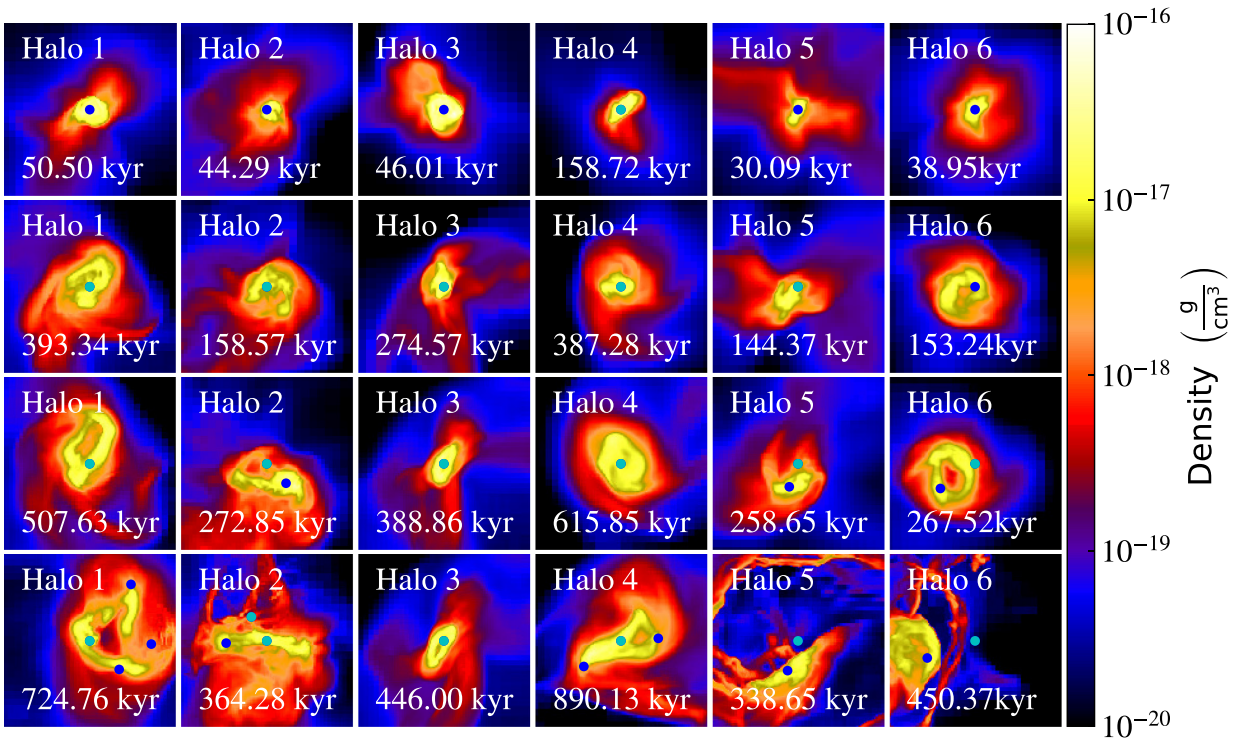


**Figure 2.** Disc evolution and SF in all six haloes. The images are density projections showing the average gas density along the line of sight and are 1 pc on a side. Dark blue dots are stars with masses $\geq 10\ M_\odot$ and cyan dots are stars with masses $\geq 1000\ M_\odot$. Each column shows the disc evolution in one halo.

those in isothermal atomically-cooled haloes in much higher LW backgrounds.

### 3.3 Disc evolution/star formation

Discs in our simulations remain stable most of the times with Toomre $Q > 1$, but occasionally become unstable and lead to SF in Jeans unstable cells at the minima of local gravitational potential. Overall, we find that multiple stars form in almost all simulations, but they get merged on short time-scales of a few kyr in agreement with previous studies exploring such conditions (Safranek-Shrader et al. 2012; Latif et al. 2014c). As shown in Fig. 2, collapse leads to the formation of thick, rotationally flattened discs with initial radii of ∼0.1 pc and masses of a few thousand solar masses. They grow to ∼0.2–0.3 pc in radius by the end of the runs at nearly 1 Myr. These discs are a factor of five smaller in radius than those in isothermal atomically cooled flows at similar times because of lower infall rates due to less efficient $H_2$ cooling. At later times the discs develop irregular features created by ionizing UV feedback, as we discuss in greater detail below.

A single star particle with a mass of a few solar masses forms first at the center of each disc when it reaches densities of $\sim 10^{-16}$ g cm$^{-3}$. Although new star particles can form within the accretion radius of this star at times and merge with it a few hundred or thousand years later, it mostly grows by accretion of dense gas. Secondary stars begin to appear by ∼250 kyr in H2, H5, and H6 at ∼ 500 kyr in H1 and at ∼ 700 kyr in H4. At the end of the run H1, H4, and H5 host four stars, H2 has three, and H6 has two. H3 forms a few low-mass stars, but they are subsumed into the central star and only it remains at the end of the run at 900 kyr. Most of the additional stars have masses of a few tens to hundreds of solar masses, as shown in Table 1.

### 3.4 Radiative feedback

Because accretion on to the main star begins at rates of a few $10^{-3}\ M_\odot\ yr^{-1}$ in all six haloes (on par with normal Pop III star-forming haloes; Latif et al. 2013c; Hosokawa et al. 2016), it is initially treated as a hot blue source of ionizing photons. The recombination times in the vicinity of the stars are about 100 yr, therefore the UV flux remains trapped deep in the disc. However, the energy deposition mainly by UV ionizing radiation from the central star creates dumbbell shaped centric outflows which clear the gas from some of the discs, creating the annular structures and cavities in the discs shown in Fig. 2. Stellar feedback lowers the density in the surroundings ($\sim 10^{-20}$ g cm$^{-3}$), where highly anisotropic H II regions can break out along the lines of sight with lower column densities. The temperatures and ionization fractions in the H II regions around the central stars are shown in Figs 3–5, they have temperatures of $2 \times 10^4$ K and HII fractions very close to 1.0. In H2, H5, and H6 H II regions break out around the central stars at 330 kyrs, 260 kyrs, and 400 kyrs, respectively. The I-front blowouts evacuate gas from the vicinity of the main stars in these three haloes and terminate their growth. In H3 the H II region forms around the primary star at 120 kyrs and gets detached from the star. In H1 and H4 compact H II regions around the central star get trapped (size of 0.05 pc), and consequently the mass accretion rate on to stars plummets momentarily but H II regions expand around secondary stars at 600 and 800 kyrs, respectively. In these haloes overall energy deposition due to the stellar feedback only declines mass accretion on to the primary stars by an order of magnitude. For the central stars, sizes of the Stromgren radii ($R_S$) vary from 0.6 to 3.0 pc due to the anisotropic gas distribution around them and the corresponding Bondi radii ($R_B$) are 1.7–2.0 pc. Along the lines of sight with lower column densities $R_S$ becomes larger than $R_B$ and H II regions break out; see also Inayoshi, Haiman & Ostriker (2016).

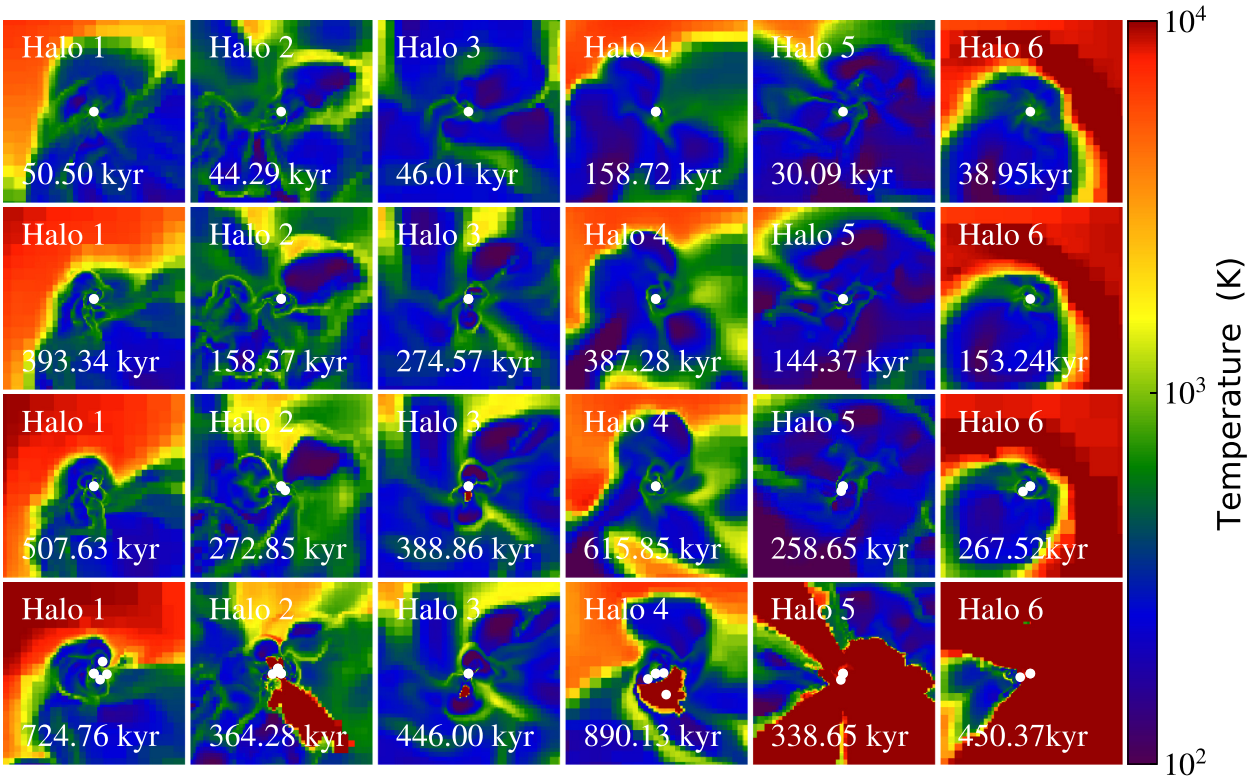


**Figure 3.** Temperature slices of the central 5 pc of the halo, taken along the *x*-axis.

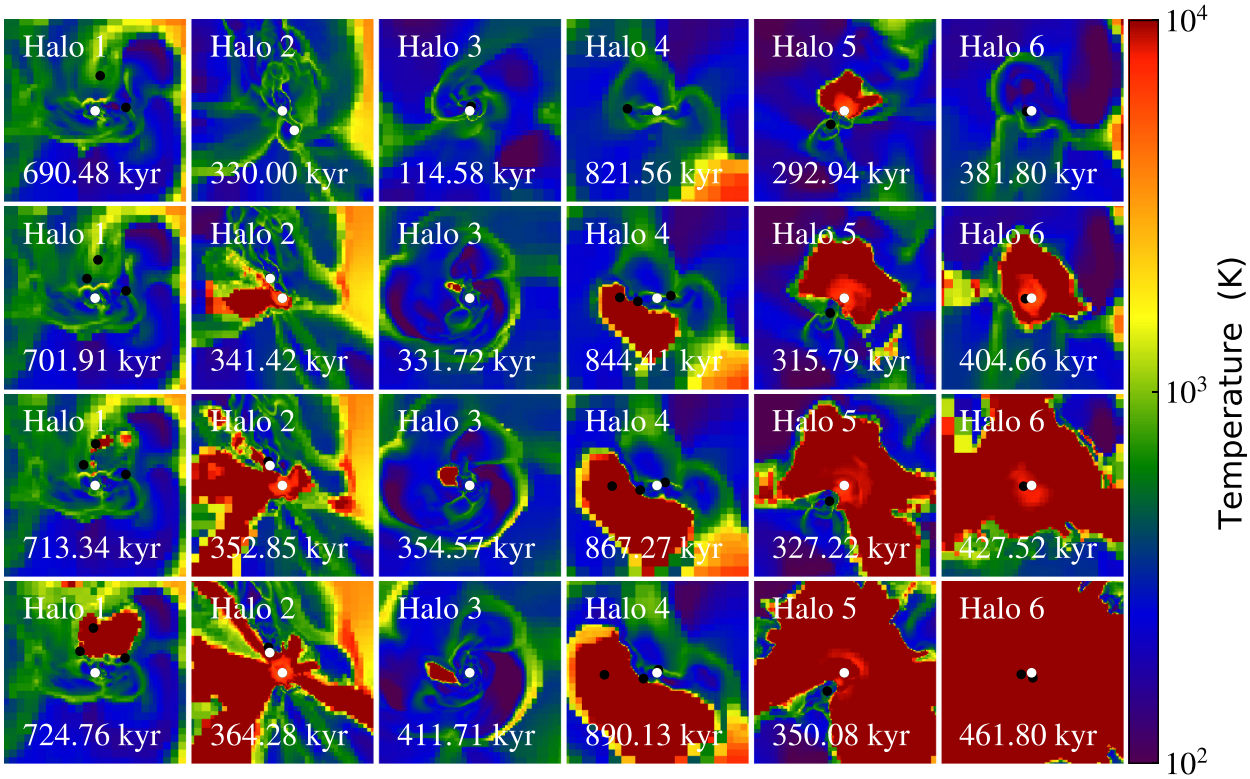


**Figure 4.** The temperature around massive stars is shown in the central 2 pc of the halo by taking slices along *y*-axis. In each column we show epochs at the onset and breakout of H II regions corresponding to the sharp drops in the mass accretion rates on to stars ($< 0.001$ $M_\odot$ $yr^{-1}$). The white dots are stars with masses $\geq 1000$ $M_\odot$ and black dots are stars with masses $\geq 10$ $M_\odot$.

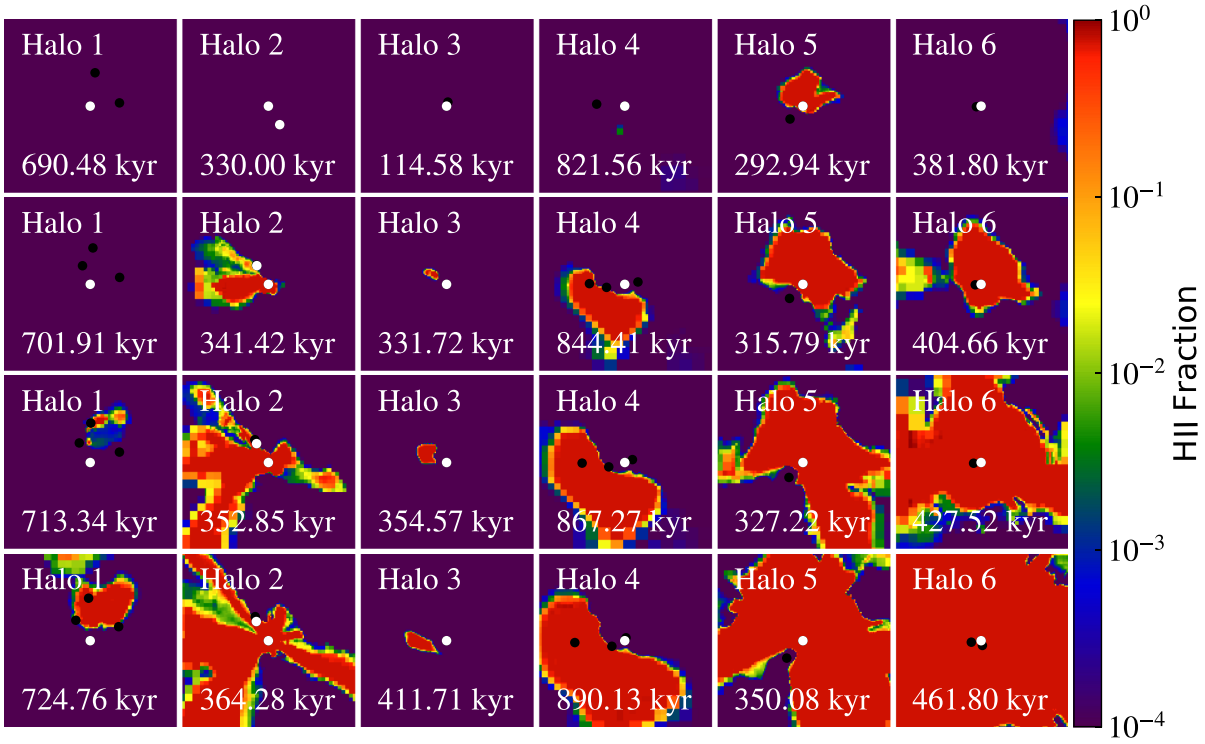


**Figure 5.** The H II fraction around massive stars is shown in the central 2 pc of the halo by taking slices along *y*-axis. In each column we show epochs at the onset and breakout of H II regions corresponding to the sharp drops in the mass accretion rates on to stars ($< 0.001$ $M_\odot$ $yr^{-1}$).The white dots are stars with masses $\geq 1000$ $M_\odot$ and black dots are stars with masses $\geq 10$ $M_\odot$.

Conversely, at earlier times $R_S < R_B$ (0.006–0.05 pc versus 0.09–1.07 pc) for stars with masses of 40–500 solar so the H II region cannot grow. Its later expansion is therefore mainly due to the rise in luminosity of the star as it grows by accretion.

To better quantify accretion in the midst of radiative outflows from the discs, we plot spherically averaged mass inflow ($4\pi R^2 \rho \overline{v_{rad}^-}$) and outflow ($4\pi R^2 \rho \overline{v_{rad}^+}$) rates through radial shells in each halo in Fig. 6. Inflow rates average $\sim$0.01 $M_\odot$ $yr^{-1}$ at 1 pc and fall to $10^{-4}$ $M_\odot$ $yr^{-1}$ in the vicinity of the main star. Outflows dominate inflows in H2, H5, and H6 due to I-front breakout from the disc. In H3 and H4, outflow rates exceed inflow rates at pc scales at later times. In general, outflow rates are either greater than or comparable to inflow rates within $\sim$1 pc of the star in most of the haloes. They rise over time, can be quite intermittent, and vary from halo to halo. Inflow rates fall steeply in the 0.2 pc region around stars due to stellar feedback, therefore accretion on to stars is expected to be low at later times. In the midst of inflows, we estimated the outflow rates shown in Fig 6 based on $4\pi R^2 \rho \overline{v_{rad}^+}$, but the local expansion of the gas due to turbulence, shocks, and even disc dynamics may contribute to outflows, although their contribution is an order of magnitude lower compared to the H II regions.

We show spherically averaged profiles of density, enclosed mass, temperature, and $H_2$ mass fraction at the end of our simulations in Fig. 7. In haloes H1, H3, and H4, the mean densities in the center of the halo have decreased by a factor of a few and the profile has become flattened in the central 0.5 pc because of the stellar feedback. In H2, H5, and H6 densities have fallen by about six orders of magnitude where shocked ionized flows in the H II region of the star have driven gas out of the core of the halo. Average temperatures in this region have likewise risen above $10^4$ K because of photoionizations. $H_2$ mass fractions have fallen by a few orders in magnitude because of photodissociation and collisional dissociation by free electrons. The latter can be important at early stages of H II region formation. The anisotropic H II region of the 1168 $M_\odot$ star is at an average temperature of 7000 K and has densities and $H_2$ mass fractions that are a few orders of magnitude lower than the surrounding central 0.2 pc of the halo. Average temperatures in the rest of the haloes are a few hundred Kelvin and $H_2$ abundances are a few $10^{-3}$ due to episodic recombination of ionized gas.

The small bumps in the $H_2$ profiles at $\sim$0.2 pc and 0.4 pc in H5 and H6 are due to rapid $H_2$ formation in the outer layers of the I-front. The inclusion of multiple ionizing photon energies in the spectrum of the star leads to the broadening of the front, and its outer layers can fall to ionization fractions of 10 per cent and gas temperatures of 1000–2000 K, which are prime conditions for $H_2$ formation in the gas phase via the $H^-$ channel (Ricotti, Gnedin & Shull 2001; Whalen & Norman 2008). The larger bumps in $H_2$ abundance at $\sim$1 pc in H5 and H6 arise because the dense shell of gas swept up by the D-type I-front behind them partly shields them from LW radiation from the star. Approximately 1000 $M_\odot$ of gas resides within the central 1 pc in all six haloes.

### 3.5 Accretion rates/final stellar masses

Masses and accretion rates for the main star and next most massive star in each halo are shown in Fig. 8. Accretion rates begin at a few $10^{-3}$ $M_\odot$ $yr^{-1}$, rise to a few $10^{-2}$ $M_\odot$ $yr^{-1}$, and then fall by an order of magnitude as the stars grow in mass and luminosity. High densities, ram pressures, and short recombination times in the vicinity of the star confine its H II region close to its surface and allow accretion

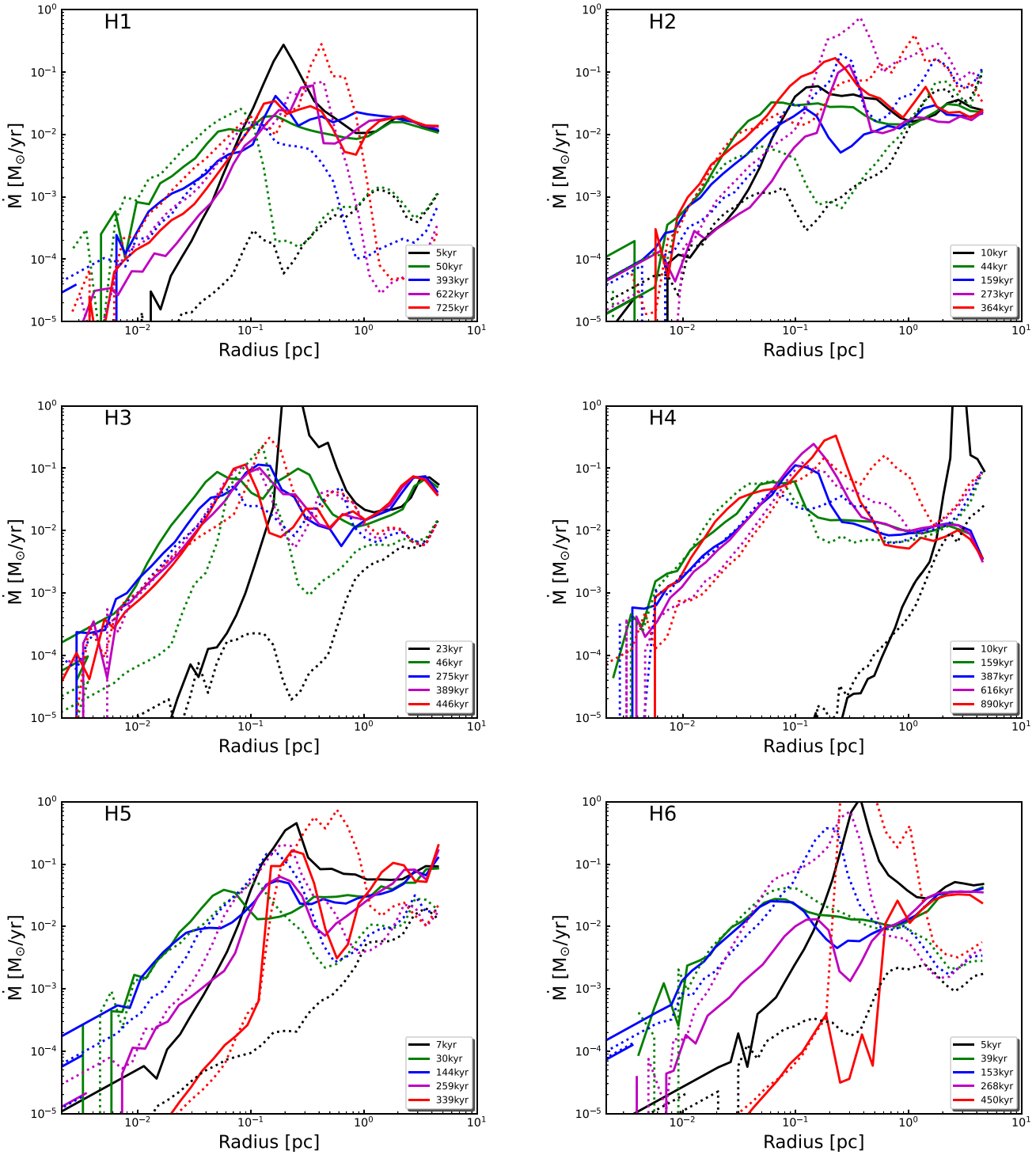


**Figure 6.** Time evolution of spherically averaged gas inflow and outflow rates in radial shells centred on the most massive star in each halo. Time is calculated from the formation of the first star in each simulation. Solid lines are inflow rates and dotted lines are outflow rates. Upper left: H1, 100 $J_{21}$; upper right: H2, 500 $J_{21}$; center left: H3, 100 $J_{21}$; center right: H4, 500 $J_{21}$; bottom left: H5, 100 $J_{21}$; bottom right: H6, 500 $J_{21}$.

to proceed for a few hundred kyr in all six haloes. In H1, an H II region never develops and the star continues to accrete at a few $10^{-3}$ $M_\odot$ $yr^{-1}$ until it reaches a mass of 2775 $M_\odot$ at the end of the run at 719 kyr. In H2 radiation from the central star terminates its growth 330 kyr after formation at a mass of 1770 $M_\odot$. But another star forms at 100 kyr and grows through mergers with other star particles and accretion until it reaches a mass of 8670 $M_\odot$ at the end of the simulation at 354 kyr. The two stars produce the highly anisotropic H II region at 354 kyr .

The star in H3 initially grows faster than those in the other haloes, with peak accretion rates of 0.03 $M_\odot$ $yr^{-1}$ over the first 20 kyr. The large drop in rate at about 100 kyr is due to strong radiatively driven

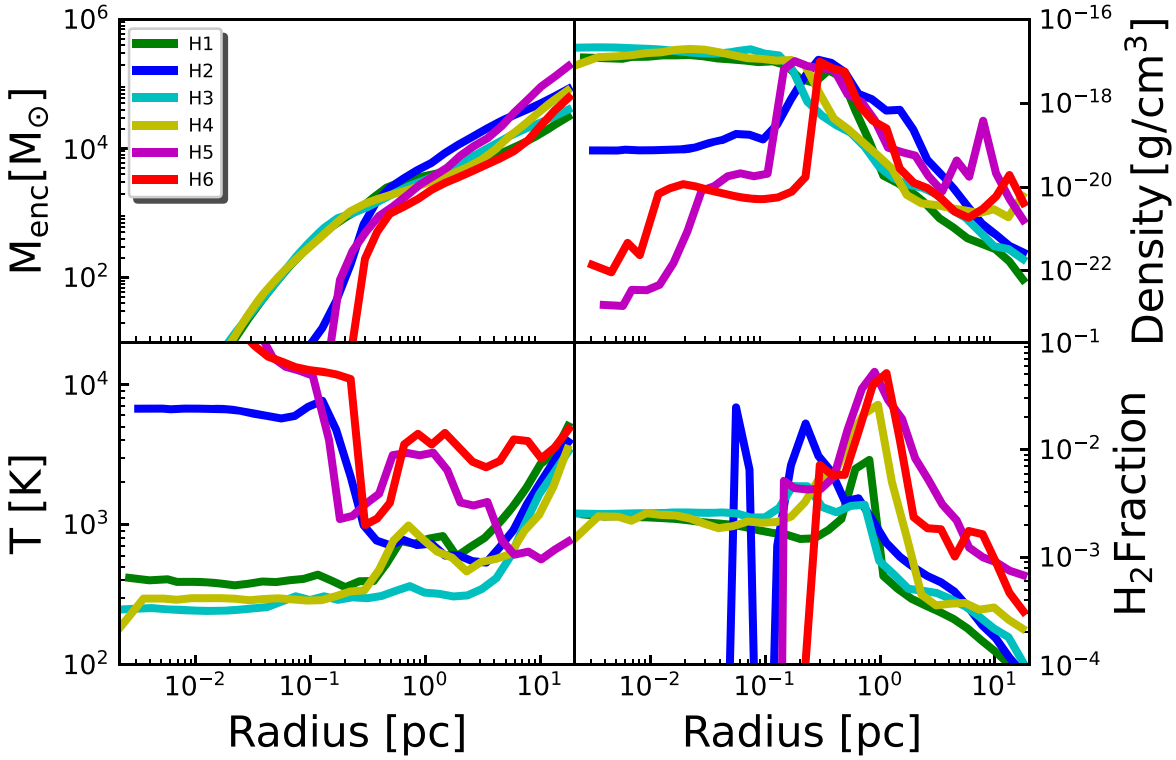


**Figure 7.** Spherically averaged densities, temperatures, enclosed masses, and $H_2$ mass fractions at the end of each run. Green, blue, cyan, yellow, magenta, and red colours are H1, H2, H3, H4, H5, and H6, respectively.

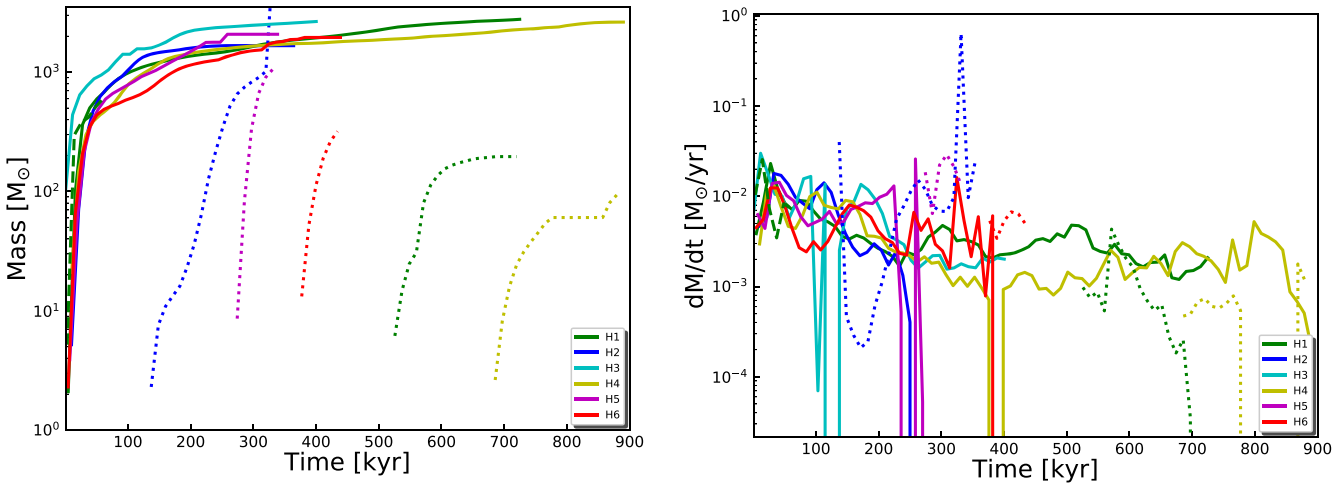


**Figure 8.** Accretion rates and masses of the two most massive stars in each halo. The green, blue, cyan, yellow, magenta, and red lines are H1, H2, H3, H4, H5, and H6, respectively. The solid lines are for the most massive stars and the dotted lines are for the second most massive star. The dashed green line is for H1 at a resolution of 75 au evolved to 57 kyr.

outflows. The mass of the star at the end of the run is 2743 $M_\odot$, having accreted at an average rate of 0.003 $M_\odot$ yr$^{-1}$. Average accretion rates for the main star in H4 are similar, ∼0.003 $M_\odot$ yr$^{-1}$, and it reaches a mass of 2638 $M_\odot$ 890 kyr after formation. The sharp dips in rate at 400 kyr and 850 kyr correspond to strong outflows that drive dense gas away from the star, the latter of which is visible in the temperature image at 880 kyr in Fig. 3. In H5 and H6, the initial growth of the stars is comparable to those in the other haloes, but at 270 kyr and 400 kyr the H II region breaks out of the disc and accretion on to the stars plummets. The final mass of the central star in H5 and H6 is 2079 $M_\odot$ and 1955 $M_\odot$, respectively.

Overall, accretion on to the stars is intermittent and falls by a few orders in magnitude during outflows. The most massive stars are 1700–2800 $M_\odot$ and, given the flattening in all the mass profiles, are unlikely to grow beyond a few thousand solar masses. This is true of the stars in H1 and H4, which were evolved for twice as long as

the others (719 and 880 kyrs, respectively), but grew in mass by less than a factor of two after their profiles flattened out. The second most massive stars have typical masses of about 100 $M_\odot$, are born in the last 100–200 kyr, and have accretion rates of $\sim$0.001 $M_\odot$ $yr^{-1}$. The masses of all stars in our simulations are listed in Table 1.

The maximum resolution in our simulation is 300 au so we cannot resolve protostellar discs around individual stars. However, even if fragmentation occurs on smaller scales the clump migration time-scale is shorter than the Kelvin–Helmholtz time-scale at higher densities. Clumps are therefore expected to migrate inwards and merge with the central object (Latif & Schleicher 2015). We resimulated H1 with a maximum spatial resolution of 75 au (four times that of the others) and found that the most massive star grew to 600 $M_\odot$ in 57 kyr. As shown in Fig. 8, its accretion rate and growth track are quite similar to those in the original run so our results likely hold at even higher resolution.

### 3.6 Comparison with previous studies

Previous studies investigating fragmentation in massive primordial haloes under a moderate LW flux either ignored radiative feedback from stars (Safranek-Shrader et al. 2012; Latif et al. 2014c; Regan & Downes 2018b) or found it not to be important (Regan & Downes 2018b, hereafter RD18). RD18 only considered a single peculiar halo at several resolutions and LW backgrounds (1, 100, and 1000 $J_{21}$) for 250 kyr (and 500 kyr in two cases), a small fraction of the lifetimes of the stars in their models. Hence, their results are not applicable to typical haloes forming at high redshift. The halo studied by RD18 has a mass of $\sim 10^7$ $M_\odot$ and collapses at $z = 24.7$, while the haloes in our study collapse at $13 < z < 18$ except H3. To understand this difference, we plot a halo mass function at different redshifts in Fig. 9 using the analytical mass function of Warren et al. (2006). The halo mass function shows that haloes like the halo in RD18 are very rare, 0.1 halo per 1 $Mpc^3$, while the haloes in our study are a hundred times more abundant, about 10 haloes per 1 $Mpc^3$. Therefore, our haloes represent typical haloes forming at $z = 15$ and the RD18 halo is an outlier. Such haloes have triggered higher accretion rates in RD18, which resulted in larger stellar masses in their study. The average mass accretion rates on to stars in our simulations are 0.001–0.01 $M_\odot$ $yr^{-1}$ for 100 and 500 $J_{21}$ an order of magnitude lower than in RD18. We also performed one simulation with 1000 $J_{21}$ and found similar results. In fact, theoretical estimates suggest that mass accretion rates scale with sound speed $\sim c_s^3/G \sim 0.1 \times (T/8000K)^{3/2} M_\odot$ $yr^{-1}$. The gas temperature in our halo centers is about 1000 K for which the expected accretion rates are 0.004 $M_\odot$ $yr^{-1}$, in agreement with the results of our study. Therefore, we believe our accretion rates are realistic and in accordance with theoretical expectations. Stellar masses in our study are about an order of magnitude lower than those in RD18 due to the lower mass accretion rates observed in our simulations. At such accretion rates ($< 0.04$ $M_\odot$ $yr^{-1}$) stars become blue and hot in our simulations and produce strong feedback which launches outflows on parsec scales and halts accretion on to them. In contrast, higher accretion rates as in RD18 result in red and cool stars which do not produce ionizing radiation. Consequently, the mass accretion on to stars and stellar masses are an order of magnitude larger. RD18 switched off ionizing radiation in their simulations, which results in more fragmentation and three-body interactions that eject stars from the disc, terminating their growth.

We have simulated six distinct haloes here that enable us to study variations from halo to halo and followed accretion on to the stars for up to 900 kyr, four times longer than RD18. These are thus the first simulations that have followed the accretion of the resulting objects for a relevant fraction of the lifetime of the stars in the presence of ionizing radiation. They allow us to capture the quenching of accretion on to stars because of their ionizing UV flux and hence obtain more accurate final masses. We found that the final stellar masses are mainly determined by the stellar feedback. Our larger ensemble of six haloes therefore demonstrates that ionizing UV radiation from the star sets its final mass in a wide range of environments. We have explored LW backgrounds of 100–500 $J_{21}$ and found that Pop III stars of a few thousand solar masses can form in them. Our findings suggest that moderate LW fluxes cannot induce the large accretion rates ($\geq 0.04$ $M_\odot$ $yr^{-1}$) required for supermassive SF in typical haloes and massive Pop III stars of 1800–2800$M_\odot$ form under these conditions.

## 4 DISCUSSION AND CONCLUSION

We find that moderate LW backgrounds in the primordial universe led to the formation of 1800–2800 $M_\odot$ Pop III stars, intermediate in mass to those in minihaloes before such backgrounds existed (30–500 $M_\odot$; Hirano et al. 2014, 2015) and those in atomically cooled haloes in the most extreme backgrounds ($\sim 10^5$ $M_\odot$; e.g. Woods et al. 2017). Intermediate LW backgrounds enabled primordial haloes to grow to somewhat larger masses before forming stars while allowing some $H_2$ to survive in their cores. This led to a more massive gas reservoir in the center of the halo that was at higher temperatures than those normally associated with $H_2$ cooling. At the onset of collapse, Ly$\alpha$ cooling dominated in the outer regions of the halo but $H_2$ cooling regulated the collapse of the core, but at rates that were 10–50 times higher than those in minihaloes, because the higher virial temperatures were close to the peak in the $H_2$ cooling and formation rates. Supercharged $H_2$ cooling thus produced 1000–3000 $M_\odot$ Pop III stars. We find that fragmentation in haloes in moderate LW backgrounds tends to be mild so these stars are usually accompanied by a few normal Pop III stars. Our results suggest typical stellar masses of a few thousand solar for LW strengths of 100–1000 $J_{21}$. Therefore, the IMF of Pop III stars is expected to be a top heavy with the masses up to a few thousand solar masses under such conditions. They opened a third channel of Pop III SF that led to the birth of intermediate mass black holes in primordial galaxies. We expect such conditions were likely common at high redshifts as the number density of these pristine haloes exposed to a given LW background strongly varies with the strength of the flux (Agarwal et al. 2014; Hartwig et al. 2015; Inayoshi & Tanaka 2015; Habouzit et al. 2016). Even a factor of a few difference in LW flux changes the abundance by two orders of magnitude.

Our simulations were evolved for more than half the expected lifetimes of the stars (Schaerer 2002) and radiative feedback levels off their masses well before the end of the runs. These massive stars are expected to collapse to BHs via the photodisintegration instability (Heger & Woosley 2002; Heger et al. 2003) or He depletion in their cores without exploding (see Fig. 4 of Woods, Heger & Haemmerlé 2020). In the future stellar evolution calculations run inline with cosmological simulations will be required to determine at what masses the stars collapse to BHs. We find that radiation from the star plays a pivotal role in its evolution in intermediate LW backgrounds. Accretion rates in haloes collapsing via Ly$\alpha$ and $H_2$ cooling can be 100 times lower than those cooling by Ly$\alpha$ alone, and are close to the limit below which the stars become blue and hot rather than cool and red ($\sim$0.02 $M_\odot$ $yr^{-1}$; Herrington, Whalen & Wood (in preparation). Thus, if a star happens to be born blue in such a halo its ionizing UV radiation tends to keep it blue by

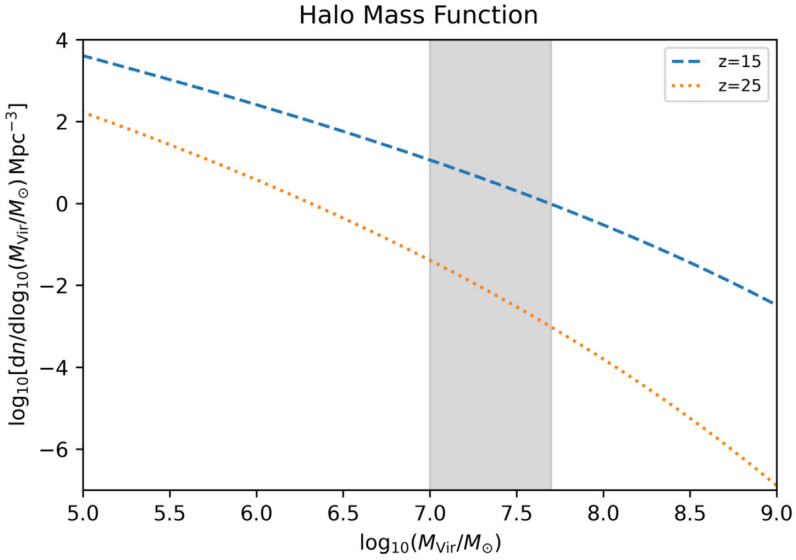


**Figure 9.** Halo mass function at different redshifts using the analytical function of Warren et al. (2006).

curtailing accretion on to it. As the star becomes more massive it becomes more luminous and drives accretion rates even lower. None of the stars in our runs ever become red, because they never reach accretion rates of 0.04 $M_\odot$ $yr^{-1}$. This rate is a little larger than those found in stellar evolution models to cause stars to become blue so the radiative feedback in our models should be taken to be an upper limit and the true masses of the stars may be somewhat higher.

We have assumed here LW backgrounds of 100 and 500 $J_{21}$ due to nearby star-forming galaxies. A stellar mass of a few times $\geq 10^6 M_\odot$ is required to provide such flux for a Salpeter IMF with mass range of 10–100 $M_\odot$ (Agarwal et al. 2012; Dijkstra, Ferrara & Mesinger 2014; Habouzit et al. 2016; Chon & Latif 2017). We assume here $T_{rad} = 10^5$ K and ignore photodetachment of $H^-$, but the spectral temperatures of the first galaxies are expected to be between $T_{rad} = 10^4$–$10^5$ K (Sugimura et al. 2014; Agarwal & Khochfar 2015; Latif et al. 2015). The LW source haloes must be located at ∼10 kpc to avoid metal pollution (Dijkstra et al. 2014; Habouzit et al. 2016) and about 60 per cent of such haloes are metal free at z = 15 (Latif et al. 2016). We have assumed here that the LW background is constant for the duration of our runs (about 200 Myr), and is provided by Pop II stars due to ongoing SF in nearby haloes. The impact of UV ionizing radiation from LW source galaxies was investigated by Chon & Latif (2017); they found that most of it is absorbed by the filaments and dense clumps surrounding the source galaxy. In some cases, ionizing radiation from the source galaxy actually promotes the collapse of the atomically cooling halo (see also Johnson et al. 2014). The LW sources may also emit X-rays produced by the X-ray binaries or even massive stars. X-rays heat gas at low densities, but also enhance ionization fractions that catalyse $H_2$ formation. These effects have been investigated by Jeon et al. (2012), Inayoshi & Omukai (2012), and Latif et al. (2015), who found that X-rays are attenuated at higher densities and do not impact the characteristic masses of stars (Hummel et al. 2015). Therefore, we expect that ionizing UV and X-rays from nearby sources will not have much impact on our findings.

Our accretion recipe is based on the mass influx through the accretion sphere and we assumed an accretion radius of four cells. Since the Jeans length must be resolved by at least four cells in order to avoid spurious fragmentation (Truelove et al. 1997), the accretion radius of sink particles must not be smaller than two grid cells; see also Federrath et al. (2010). We performed an additional simulation (shown in Fig. 8) with an accretion radius that was four times smaller and found similar stellar masses. Therefore, we do not believe that the choice of the accretion radius has a strong impact on our results. However, current computational constraints do not allow us to resolve flows all the way down to the surface of the star in cosmological simulations, so our stellar masses should be taken to be upper limits. Instead of using an instantaneous accretion rate, we use accretion rates averaged over 1 kyr intervals and never cap the rates, but they never exceed 0.03 $M_\odot yr^{-1}$ in our runs.

We selected six distinct haloes and turned on LW backgrounds of strengths 100 $J_{21}$ for H1, H3, and H5 and 500 $J_{21}$ for H2, H4, and H6. This allowed us to robustly estimate the upper limit of stellar mass irrespective of their merger history and environments. Our results confirm that the upper limit of stellar mass is determined by its feedback irrespective of the strength of the LW flux and the halo mass range explored here. Therefore, if we turn on LW backgrounds of different strengths for the same halo, the results are expected to be similar. Less fragmentation occurs in our models than in simulations of normal Pop III SF (Turk, Abel & O'Shea 2009; Clark et al. 2011; Greif et al. 2012; Susa, Hasegawa & Tominaga 2014; Latif et al. 2015; Hosokawa et al. 2016; Stacy, Bromm & Lee 2016; Susa 2019; Sugimura et al. 2020). Even though SF in our haloes is also regulated by $H_2$ cooling, the gas at the center of the disc is several times hotter so it is better supported by thermal pressure against fragmentation. In reality, most simulations of atomic collapse performed to date probably overestimate fragmentation because they ignore magnetic fields that likely arose in most primordial haloes because of subgrid turbulent dynamos (Schober et al. 2012; Turk et al. 2012; Latif et al. 2013a; Latif, Schleicher & Schmidt 2014a; Sharda, Federrath & Krumholz 2020). Such fields would tend to stabilize the disc and suppress fragmentation.

It is not clear if the extremely massive Pop III stars in our simulations could later evolve into the first quasars, because Smidt et al. (2018) found that they must be seeded by BHs of at least $10^5$ $M_\odot$ at $z \sim 20$ to reach $10^9$ $M_\odot$ by $z \sim 7$ in the cold accretion flows that are thought to fuel their growth (see also Latif & Khochfar

2020). If not, they could instead yield a population of less-massive lower luminosity quasars that are yet to be discovered. Synergies between *JWST* and *Euclid* or the *RST* could reveal the existence of these objects when they inaugurate the era of $5 < z < 15$ quasar astronomy in the coming decade.

## ACKNOWLEDGEMENTS

MAL thanks the UAEU for funding via UPAR grant No. 31S390. DRGS thanks for funding via the Chilean BASAL Centro de Excelencia en Astrofisica y Tecnologias Afines (CATA) grant PFB-06/2007. DRGS acknowledges financial support from Millenium Nucleus NCN19_058 (TITANs).

## 5 DATA AVAILABILITY STATEMENT

The data underlying this article will be shared on reasonable request to the corresponding author.

## REFERENCES

Abel T., Anninos P., Zhang Y., Norman M. L., 1997, New Astron., 2, 181
Agarwal B., Khochfar S., 2015, MNRAS, 446, 160
Agarwal B., Khochfar S., Johnson J. L., Neistein E., Dalla Vecchia C., Livio M., 2012, MNRAS, 425, 2854
Agarwal B., Dalla Vecchia C., Johnson J. L., Khochfar S., Paardekooper J.-P., 2014, MNRAS, 443, 648
Agarwal B., Regan J., Klessen R. S., Downes T. P., Zackrisson E., 2017, MNRAS, 470, 4034
Agarwal B., Cullen F., Khochfar S., Ceverino D., Klessen R. S., 2019, MNRAS, 488, 3268
Alvarez M. A., Wise J. H., Abel T., 2009, ApJ, 701, L133
Ardaneh K., Luo Y., Shlosman I., Nagamine K., Wise J. H., Begelman M. C., 2018, MNRAS, 479, 2277
Bañados E. et al., 2018, Nature, 553, 473
Becerra F., Greif T. H., Springel V., Hernquist L. E., 2015, MNRAS, 446, 2380
Becerra F., Marinacci F., Bromm V., Hernquist L. E., 2018, MNRAS, 480, 5029
Boekholt T. C. N., Schleicher D. R. G., Fellhauer M., Klessen R. S., Reinoso B., Stutz A. M., Haemmerlé L., 2018, MNRAS, 476, 366
Bromm V., Loeb A., 2003, ApJ, 596, 34
Bryan G. L. et al., 2014, ApJS, 211, 19
Chon S., Latif M. A., 2017, MNRAS, 467, 4293
Chon S., Hosokawa T., Yoshida N., 2018, MNRAS, 475, 4104
Clark P. C., Glover S. C. O., Smith R. J., Greif T. H., Klessen R. S., Bromm V., 2011, Science, 331, 1040
Davis A. J., Natarajan P., 2009, MNRAS, 393, 1498
Devecchi B., Volonteri M., 2009, ApJ, 694, 302
Dijkstra M., Ferrara A., Mesinger A., 2014, MNRAS, 442, 2036
Federrath C., Banerjee R., Clark P. C., Klessen R. S., 2010, ApJ, 713, 269
Greif T. H., White S. D. M., Klessen R. S., Springel V., 2011, ApJ, 736, 147
Greif T. H., Bromm V., Clark P. C., Glover S. C. O., Smith R. J., Klessen R. S., Yoshida N., Springel V., 2012, MNRAS, 424, 399
Habouzit M., Volonteri M., Latif M., Dubois Y., Peirani S., 2016, MNRAS, 463, 529
Haemmerlé L., Woods T. E., Klessen R. S., Heger A., Whalen D. J., 2018a, MNRAS, 474, 2757
Haemmerlé L., Woods T. E., Klessen R. S., Heger A., Whalen D. J., 2018b, ApJ, 853, L3
Hahn O., Abel T., 2011, MNRAS, 415, 2101
Haiman Z., 2013, in Wiklind T., Mobasher B., Bromm V., eds, Astrophysics and Space Science Library, Vol. 396, The Formation of the First Massive Black Holes. Springer, Berlin, p. 293
Hartwig T., Glover S. C. O., Klessen R. S., Latif M. A., Volonteri M., 2015, MNRAS, 452, 1233
Heger A., Woosley S. E., 2002, ApJ, 567, 532
Heger A., Fryer C. L., Woosley S. E., Langer N., Hartmann D. H., 2003, ApJ, 591, 288
Hirano S., Hosokawa T., Yoshida N., Umeda H., Omukai K., Chiaki G., Yorke H. W., 2014, ApJ, 781, 60
Hirano S., Hosokawa T., Yoshida N., Omukai K., Yorke H. W., 2015, MNRAS, 448, 568
Hosokawa T., Yorke H. W., Inayoshi K., Omukai K., Yoshida N., 2013, ApJ, 778, 178
Hosokawa T., Hirano S., Kuiper R., Yorke H. W., Omukai K., Yoshida N., 2016, ApJ, 824, 119
Hummel J. A., Stacy A., Jeon M., Oliveri A., Bromm V., 2015, MNRAS, 453, 4136
Inayoshi K., Omukai K., 2012, MNRAS, 422, 2539
Inayoshi K., Tanaka T. L., 2015, MNRAS, 450, 4350
Inayoshi K., Haiman Z., Ostriker J. P., 2016, MNRAS, 459, 3738
Inayoshi K., Visbal E., Haiman Z., 2019, Annu. Rev., 58, 27
Jeon M., Pawlik A. H., Greif T. H., Glover S. C. O., Bromm V., Milosavljević M., Klessen R. S., 2012, ApJ, 754, 34
Johnson J. L., Whalen D. J., Li H., Holz D. E., 2013, ApJ, 771, 116
Johnson J. L., Whalen D. J., Agarwal B., Paardekooper J.-P., Khochfar S., 2014, MNRAS, 445, 686
Latif M. A., Ferrara A., 2016, PASA, 33, e051
Latif M. A., Khochfar S., 2019, MNRAS, 490, 2706
Latif M. A., Khochfar S., 2020, MNRAS, 497, 3761
Latif M. A., Schleicher D. R. G., 2015, MNRAS, 449, 77
Latif M. A., Volonteri M., 2015, MNRAS, 452, 1026
Latif M. A., Schleicher D. R. G., Schmidt W., Niemeyer J., 2013a, MNRAS, 432, 668
Latif M. A., Schleicher D. R. G., Schmidt W., Niemeyer J., 2013b, MNRAS, 433, 1607
Latif M. A., Schleicher D. R. G., Schmidt W., Niemeyer J., 2013c, ApJ, 772, L3
Latif M. A., Schleicher D. R. G., Schmidt W., 2014a, MNRAS, 440, 1551
Latif M. A., Bovino S., Van Borm C., Grassi T., Schleicher D. R. G., Spaans M., 2014b, MNRAS, 443, 1979
Latif M. A., Schleicher D. R. G., Bovino S., Grassi T., Spaans M., 2014c, ApJ, 792, 78
Latif M. A., Bovino S., Grassi T., Schleicher D. R. G., Spaans M., 2015, MNRAS, 446, 3163
Latif M. A., Omukai K., Habouzit M., Schleicher D. R. G., Volonteri M., 2016, ApJ, 823, 40
Latif M. A., Khochfar S., Whalen D., 2020, ApJ, 892, L4
Luo Y., Ardaneh K., Shlosman I., Nagamine K., Wise J. H., Begelman M. C., 2018, MNRAS, 476, 3523
Madau P., Haardt F., Dotti M., 2014, ApJ, 784, L38
Maio U., Borgani S., Ciardi B., Petkova M., 2019, PASA, 36, e020
Mirocha J., Skory S., Burns J. O., Wise J. H., 2012, ApJ, 756, 94
Mortlock D. J. et al., 2011, Nature, 474, 616
O'Shea B. W., Norman M. L., 2007, ApJ, 654, 66
Patrick S., Whalen D. J., Elford J., Latif M., 2020, MNRAS, preprint (arXiv:2012.11612v1)
Planck Collaboration XIII, 2016, A&A, 594, A13
Regan J. A., Downes T. P., 2018a, MNRAS, 475, 4636
Regan J. A., Downes T. P., 2018b, MNRAS, 478, 5037
Regan J. A., Haehnelt M. G., 2009, MNRAS, 393, 858
Regan J. A., Johansson P. H., Wise J. H., 2014, ApJ, 795, 137
Regan J. A., Wise J. H., Woods T. E., Downes T. P., O'Shea B. W., Norman M. L., 2020, The Open Journal of Astrophysics, 3, 15
Reinoso B., Schleicher D. R. G., Fellhauer M., Klessen R. S., Boekholt T. C. N., 2018, A&A, 614, A14
Ricotti M., Gnedin N. Y., Shull J. M., 2001, ApJ, 560, 580
Safranek-Shrader C., Agarwal M., Federrath C., Dubey A., Milosavljević M., Bromm V., 2012, MNRAS, 426, 1159
Sakurai Y., Yoshida N., Fujii M. S., Hirano S., 2017, MNRAS, 472, 1677
Schaerer D., 2002, A&A, 382, 28

Schauer A. T. P., Regan J., Glover S. C. O., Klessen R. S., 2017, MNRAS, 471, 4878
Schleicher D. R. G., Palla F., Ferrara A., Galli D., Latif M., 2013, A&A, 558, A59
Schober J., Schleicher D., Federrath C., Glover S., Klessen R. S., Banerjee R., 2012, ApJ, 754, 99
Sharda P., Federrath C., Krumholz M. R., 2020, MNRAS, 497, 336
Smidt J., Whalen D. J., Johnson J. L., Surace M., Li H., 2018, ApJ, 865, 126
Smith A., Becerra F., Bromm V., Hernquist L., 2017, MNRAS, 472, 205
Smith B. D., Regan J. A., Downes T. P., Norman M. L., O'Shea B. W., Wise J. H., 2018, MNRAS, 480, 3762
Stacy A., Bromm V., Loeb A., 2011, ApJ, 730, L1
Stacy A., Bromm V., Lee A. T., 2016, MNRAS, 462, 1307
Suazo M., Prieto J., Escala A., Schleicher D. R. G., 2019, ApJ, 885, 127
Sugimura K., Omukai K., Inoue A. K., 2014, MNRAS, 445, 544
Sugimura K., Matsumoto T., Hosokawa T., Hirano S., Omukai K., 2020, ApJ, 892, L14
Susa H., 2019, ApJ, 877, 99
Susa H., Hasegawa K., Tominaga N., 2014, ApJ, 792, 32
Truelove J. K., Klein R. I., McKee C. F., Holliman II J. H., Howell L. H., Greenough J. A., 1997, ApJ, 489, L179+
Tseliakhovich D., Hirata C., 2010, Phys. Rev. D, 82, 083520
Turk M. J., Abel T., O'Shea B., 2009, Science, 325, 601
Turk M. J., Oishi J. S., Abel T., Bryan G. L., 2012, ApJ, 745, 154
Umeda H., Hosokawa T., Omukai K., Yoshida N., 2016, ApJ, 830, L34
Volonteri M., 2010, A&AR, 18, 279
Volonteri M., Silk J., Dubus G., 2015, ApJ, 804, 148
Warren M. S., Abazajian K., Holz D. E., Teodoro L., 2006, ApJ, 646, 881
Whalen D. J., Fryer C. L., 2012, ApJ, 756, L19
Whalen D., Norman M. L., 2008, ApJ, 673, 664
Whalen D., Abel T., Norman M. L., 2004, ApJ, 610, 14
Wise J. H., Abel T., 2011, MNRAS, 414, 3458
Wise J. H., Turk M. J., Abel T., 2008, ApJ, 682, 745
Wolcott-Green J., Haiman Z., Bryan G. L., 2011, MNRAS, 418, 838
Woods T. E. et al., 2019, PASA, 36, e027
Woods T. E., Heger A., Whalen D. J., Haemmerlé L., Klessen R. S., 2017, ApJ, 842, L6
Woods T. E., Heger A., Haemmerlé L., 2020, MNRAS, 494, 2236
Wu X.-B. et al., 2015, Nature, 518, 512
Yang J. et al., 2020, ApJ, 897, L14
Zhu Q., Li Y., Li Y., Maji M., Yajima H., Schneider R., Hernquist L., 2020, preprint (arXiv:2012.01458)

This paper has been typeset from a TEX/LATEX file prepared by the author.